Journal of Power Sources 196 (2011) 8719–8727

Contents lists available at ScienceDirect

Journal of Power Sources

journal homepage: www.elsevier.com/locate/jpowsour

A transmission electron microscopy study of crack formation and propagation in electrochemically cycled graphite electrode in lithium-ion cells

Sandeep Bhattacharya*, A. Reza Riahi, Ahmet T. Alpas

Department of Mechanical, Automotive and Materials Engineering, University of Windsor, 401 Sunset Avenue, Windsor, Ontario, Canada N9B 3P4

ARTICLE INFO

Article history:
Received 19 April 2011
Received in revised form 27 May 2011
Accepted 28 May 2011
Available online 6 June 2011

Keywords:
Graphite
Lithium-ion
Subsurface damage
Cyclic voltammetry
Crack formation
Transmission electron microscope

ABSTRACT

Subsurface defects and local compositional changes that occurred in graphite anodes subjected to cyclic voltammetry tests (vs. Li/Li^+, using an electrolyte consisting of 1 M $LiClO_4$ in a 1:1 volumetric mixture of ethylene carbonate and 1,2-dimethoxy ethane) were investigated using high-resolution transmission electron microscopy (HR-TEM). Cross-sections of anodes prepared by focused ion beam (FIB) milling indicated that graphite layers adjacent to solid electrolyte (SEI)/graphite interface exhibited partial delamination due to the formation of interlayer cracks. The SEI layer formed on the graphite surface consisted of Li_2CO_3 that was identified by {1 1 0} and {0 0 2} crystallographic planes. Lithium compounds, LiC_6, Li_2CO_3 and Li_2O, were observed on the surfaces of separated graphite layers. Deposition of these co-intercalation compounds near the crack tip caused partial closure of propagating graphite cracks during electrochemical cycling, and possibly reduced the crack growth rate. Graphite fibres that were observed to bridge crack faces likely provided an additional mechanism for the retardation of crack propagation.
© 2011 Elsevier B.V. All rights reserved.

1. Introduction

Understanding lithium intercalation processes that occur in graphite negative electrodes is of considerable importance for enhancing the performance of rechargeable lithium-ion batteries [1–6]. Graphite is the preferred anode material as it offers high voltages of 3–4 V when used against commercial cathodes, e.g. $LiCoO_2$, $LiMn_2O_4$, or $LiFePO_4$. Graphite has high lithium storage capacity (theoretically each Li atom co-ordinates with six C atoms). The volume change of graphite during the intercalation/de-intercalation process is typically in the order of 12% and hence not severe. Yet, graphite electrodes exhibit a drastic capacity drop, especially during the initial stages of the electrochemical process. The capacity drop is accompanied by surface damage, generally described as graphite exfoliation, or removal of graphite layers near the surface [7–11] and also as the detachment of graphite from the surface in the form of particulates [8,11].

Experimental studies were conducted to estimate the damage caused by lithium-ion intercalation/de-intercalation induced stresses within a graphite lattice using techniques such as Raman spectroscopy and atomic force microscopy [12,13]; these stresses were thought to cause 'surface structural disordering' by deformation of the graphene layers and breaking of the C–C bonds. The use of ex situ Raman spectroscopy [14] provided evidence for fracture and fragmentation of graphite particles during electrochemical cycling and a decrease of the average size of graphite (plate-like, $a \gg c$) crystallites. On the other hand it was suggested that the process of lithium insertion in graphite is highly dependent on the electrolyte composition, which also determines the electromechanical stability of graphite electrodes in lithium salt solutions during electrolytic decomposition [15]. The decomposition products are known to form a solid electrolyte (SEI) layer that covers the electrode's surface [16,17]. Investigations made using focused ion beam (FIB) microscopy revealed some details of the formation of the SEI layer on natural graphite spheres during galvanostatic charge/discharge tests [18]. Accordingly, the initial thickness of SEI under these testing condition was found to vary between 0.5 and 1.0 μm and had a rough, non-uniform morphology, but eventually attained a uniform thickness of approximately 1.6 μm after 24 cycles. Aurbach et al. [19] suggested a capacity-fading mechanism due to exfoliation of the graphite particles by co-intercalation of solvent molecules together with Li^+. Results of investigations conducted using a broad range of surface sensitive analytical tools, including XPS, XRD, FTIR, X-ray, and EIS [8,20,21], revealed that the degradation of graphite surfaces was facilitated when the solvent molecules present in the electrolyte become intercalated into the graphite layers adjacent to the surfaces. These studies also suggested that diffusion of electrolyte solution inside the graphite cracks would accelerate anode degradation. Similarly, gas evolution during electrolytic reduction was proposed to cause the degrada-

* Corresponding author. Tel.: +1 519 253 3000x2605; fax: +1 519 973 7085.
E-mail address: bhattacs@uwindsor.ca (S. Bhattacharya).

0378-7753/$ – see front matter © 2011 Elsevier B.V. All rights reserved.
doi:10.1016/j.jpowsour.2011.05.079

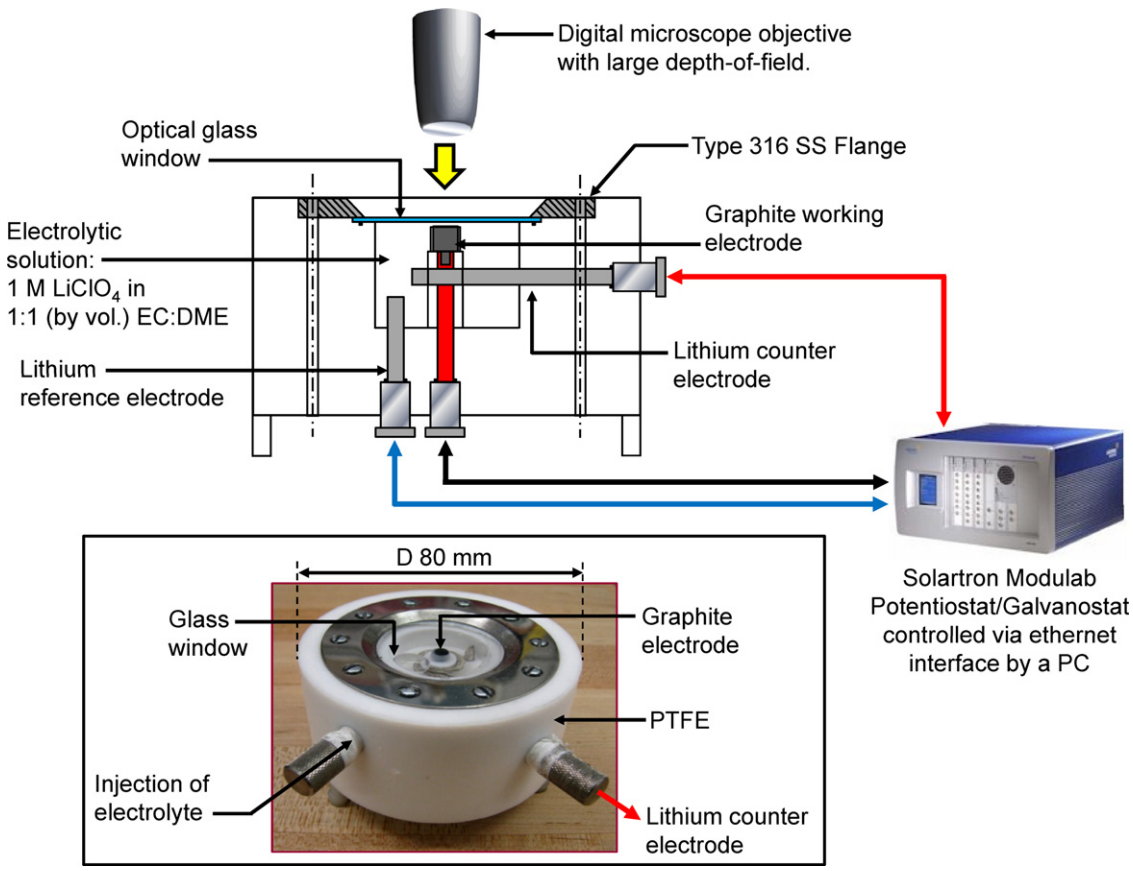

Fig. 1. Experimental set-up for in situ observation of graphite surface damage in a lithium-ion cell using a optical microscope.

tion [18]. Using in situ AFM technique, Tian et al. [22] observed volume changes as high as 204% in nano-structured $Sn_{1-x}Co_xC_y$ thin films during each charge/discharge cycle of galvanostatic tests. Harris et al. [23] performed in situ optical microscopy (90×) and by observing colour changes in graphite electrodes, induced by variations in lithium-ion concentration, predicted the diffusion rate of lithium in electrodes. Using high magnification (1000×) in situ optical microscopy, Bhattacharya et al. [24] observed the sequence of graphite surface damage events during de-lithiation, and suggested that the potential difference exerted on graphite electrode acted as the driving force for damage. It was also observed that a surface film, which formed during the lithiation stage prior to the initiation of damage, reduced the intensity of graphite degradation.

The TEM investigations shed light on the structure and composition of lithium intercalated graphite compounds and lithium distribution in the graphite lattice [25–27]. Sato et al. [28] used high resolution (HR)-TEM to investigate the difference in the microstructure between a lithium charged poly(*p*-phenylene) (PPP)-based (disordered or non-graphitic) carbon (LiC_6), formed by electrochemical cycling against lithium, and the pristine PPP-based carbon. By analyzing the fast Fourier transform (FFT) patterns, the interplanar spacing of graphite was estimated to increase by nearly 10% to 0.40 nm following lithium insertion in disordered carbon. Song et al. [26] lithiated graphite electrodes by physical contact (short circuit) with lithium foil, and studied the distribution of lithium–carbon phases using dark-field TEM imaging with SAED patterns. It was suggested that the phases can co-exist; LiC_{12} being mainly located closer to the surface, and LiC_6 was the principal phase in the bulk. Therefore, continuation of analytical HR-TEM studies are needed to better establish details of the subsurface defect structure of cycled graphite electrodes in order to understand the micromechanisms of graphite damage at the SEI/graphite interface.

Accordingly, the objective of this research was to observe subsurface defects and the local compositional changes that occurred in anodes made of graphite and subjected to cyclic voltammetry tests. These tests were well suited to study the effect of applied voltage on graphite damage. Cross-sectional FIB-milled microstructures were used to observe the morphologies of graphite cracks formed during cycling, as well as the deposition of SEI layers on the graphite anode surface and inside subsurface cracks.

2. Materials and methods

2.1. Description of electrochemical tests

Electrochemical experiments were performed using a specially designed test cell. A schematic of the experimental set-up is shown in Fig. 1, with the actual image of the electrochemical cell presented in the inset. A negative electrode made of 99.999% purity graphite (Kurt J. Lesker, Canada) with density of $1.95 \pm 0.21\ g\,cm^{-3}$ and containing traces (~10 ppm) of Al, Fe, Mg and Si was used. The graphite was micro-wire EDM machined in the shape of a cylindrical electrode with a diameter of 5 mm, and a height of 4.5 mm. The electrode was placed at the center of the electrochemical cell, which was assembled and sealed in an Ar-filled MBraun LABstar workstation with H_2O and O_2 levels maintained below 1 ppm. The electrochemical cell was constructed from polytetrafluoroethylene (PTFE), and had a quartz (optical) glass window on its top surface for graphite surface observation by an optical microscope during the test. A 99.99% pure lithium wire with a

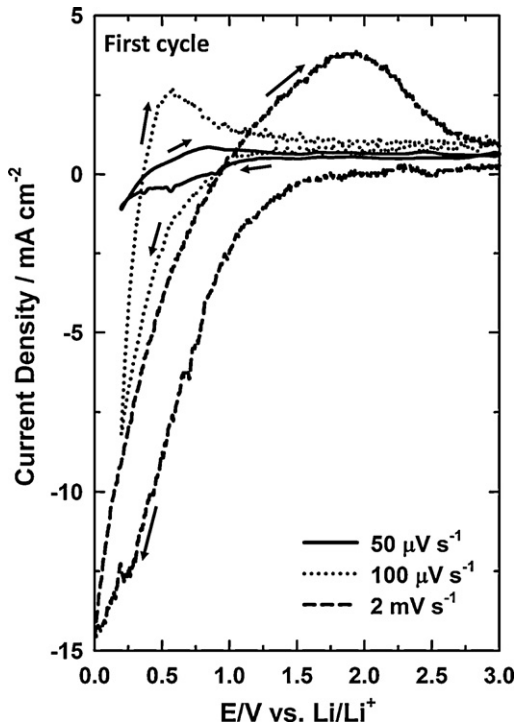

Fig. 2. Cyclic voltammetry plots for graphite electrodes showing the first cycles performed between 0.0 and 3.0 V using scan rates of 50 μV s^{-1}, 100 μV s^{-1} and 2 mV s^{-1}.

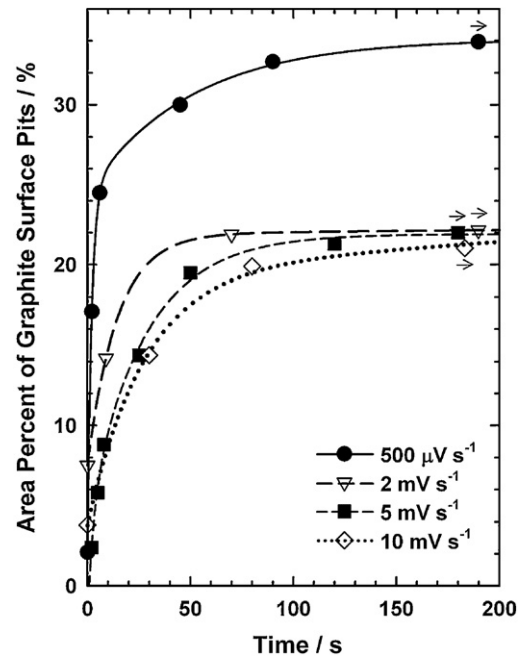

Fig. 4. Plot showing calculated area percent of cavities formed on graphite surface at different voltage scan rates. The area percentage of the surface cavities were monitored for the initial 200 s of each experiment. The arrows show no further change in area percentage until the end of the test (1000 s).

resistivity of 9.446 μΩ cm (at 20 °C) was used as the counter electrode. The reference electrode was also made of a pure lithium wire. The electrolyte solution consisted of 1 M $LiClO_4$ (99%, Alfa Aesar®) in a 1:1 (by vol.) mixture of ethylene carbonate (EC, 99%, Alfa Aesar®) and 1,2-dimethoxy ethane (DME, 99+%, stabilized with 0.01% BHT, Alfa Aesar®). The surface areas of the counter and reference lithium wires were 296 mm^2 and 95 mm^2, respectively. Prior to placing inside the cell, the surface of graphite was cleaned ultrasonically using acetone. Using Teflon, the lateral surfaces of the graphite was covered, leaving only the top surface (having an area of 19.6 mm^2) to be exposed to the electrolyte. Electrochemical tests were performed using a potentiostat/galvanostat (Solartron Modulab System) having a high-speed data acquisition rate (up to 1 MS s^{-1}).

2.2. Surface changes due to electrochemical cycling

An optical microscope with a large depth-of-field was placed directly above the glass window of the electrochemical cell and the surface of graphite was observed at 1000× magnification during the electrochemical tests providing in situ images of the surface damage events. Cyclic voltammetry (CV) tests were conducted between 0.0 and 3.0 V (vs. Li/Li$^+$) using five different scan rates between 50 μV s^{-1} and 5 mV s^{-1}. CV test data obtained from the first cycle of constant scan rate tests that were conducted at 50 μV s^{-1}, 100 μV s^{-1} and 2 mV s^{-1} (Fig. 2) show that the peak current density increased with the scan rate as expected. The graphite electrode surface was examined prior to the tests and as shown in the SEM image in Fig. 3(a), exhibited defects in the form of cavities with a diameter of 13.00 ± 4.24 μm. SEM examination of graphite electrode surfaces after the electrochemical tests (Fig. 3(b)) revealed

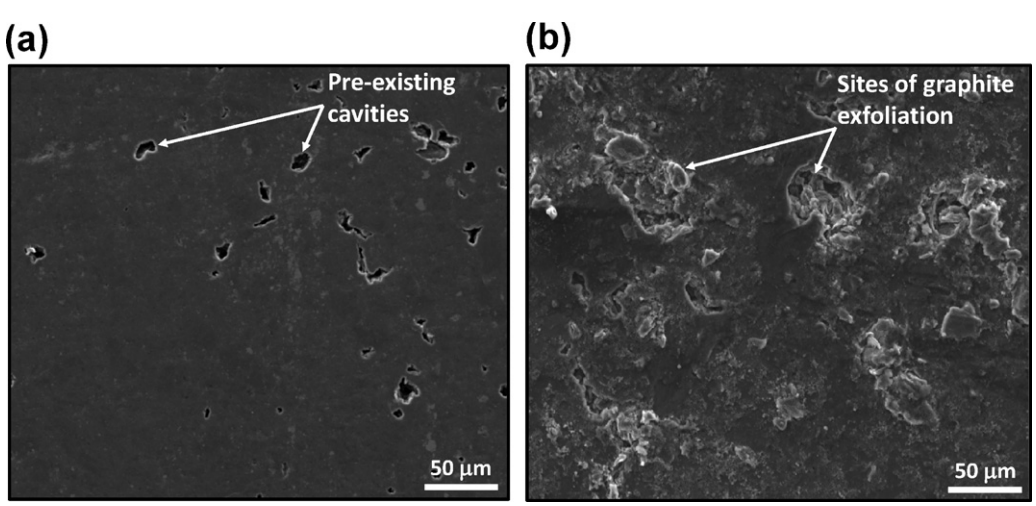

Fig. 3. SE-SEM images of graphite surfaces (a) before cycling showing the presence of natural cavities, and (b) after cycling between 0.0 and 3.0 V at a linear scan rate of 2 mV s^{-1}, revealing sites of cavities due to graphite particle removal (exfoliation).

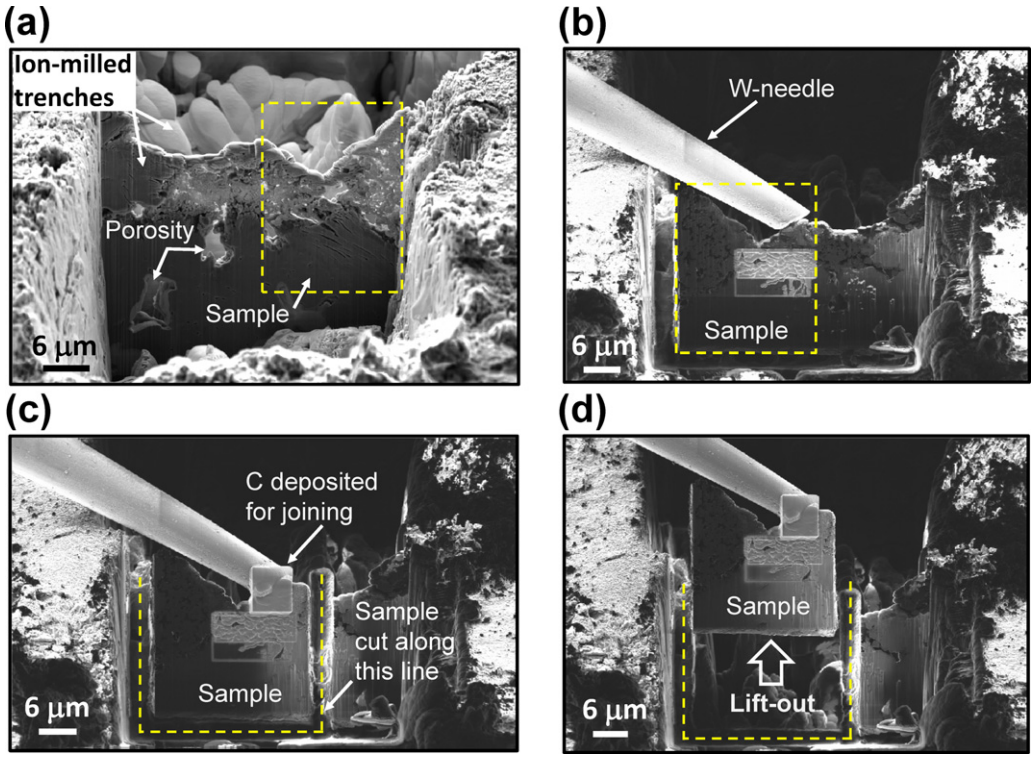

Fig. 5. SEM images illustrating the preparation steps of TEM sample by FIB "lift-out" method from a graphite electrode cycled between 0.0 and 3.0 V at a linear scan rate of 5 mV s^{-1} for 50 cycles: (a) two trenches are ion-milled at a specific location across the graphite surface to produce a thin lamella. (b) A micro-manipulator is positioned at the top of the region of interest in the lamella. (c) The tip of the micro-manipulator was welded to the membrane using a thin layer of carbon. (d) The sample is lifted out of the trench.

that the area fraction of cavities increased considerably. The pre-existing cavities acted as growth sites for the ones formed during electrochemical cycling. In addition to an increase in their number, the size of the cavities became larger during the CV tests. For example, only after the first cycle, the tests conducted at 2 mV s^{-1} produced cavities of 17.50 ± 17.67 μm in diameter and 27.50 ± 3.53 μm in depth on the graphite surface (Fig. 3(b)) due to loss of graphite from these locations.

Using quantitative metallography, the area percentage of the damaged regions formed on the cycled graphite surface was calculated and plotted in Fig. 4. It was observed that at low scan rates, e.g. at 500 μV s^{-1}, the area percent increased abruptly to 30% within the first 25 s. For a high scan rate of 10 mV s^{-1}, only 15% of the area was removed within the same time period. Thus, the majority of damage occurred during the initial stage of the experiment, and its severity increased when a low voltage scan rate was used. For tests performed between the scan rates of 2–10 mV s^{-1}, the percentage of graphite particle removed was 20% at the end of 200 s. After this initial stage the extent of surface damage occurred was at much slower rate regardless of the scan rate.

2.3. Preparation of cross-sectional TEM samples using FIB in situ lift-out technique

At the end of each test, graphite electrodes were washed in the electrolytic solution and prepared for microscopical investigations. Cross-sectional samples were excised using focused ion beam (FIB) milling technique from the locations where graphite surface damage was observed in the form of cavities. A Zeiss NVISION 40 dual beam SEM/FIB was used to investigate subsurface damage features generated in the interior of these cavities on the sections taken perpendicular to the graphite electrode surface. Care was taken to avoid potential ion-beam induced surface damage during FIB milling by depositing a 1 μm thick layer of carbon across the area where the cross-sectional cut was made. A trench was milled normal to the deposited carbon layer, using Ga^+ ions sputtered at an accelerating voltage of 30 kV, and a beam current of 80 pA. The final milling of the cross-sectional sample was conducted at a low ion-beam current of 40 pA to minimize the prospect of beam damage on the section prepared.

TEM samples were prepared using the FIB in situ "lift-out" technique. The main steps of the lift-out TEM sample preparation technique are shown in Fig. 5(a–d) and details are described. Briefly, a thin platelet of ~2 μm thickness was formed on graphite

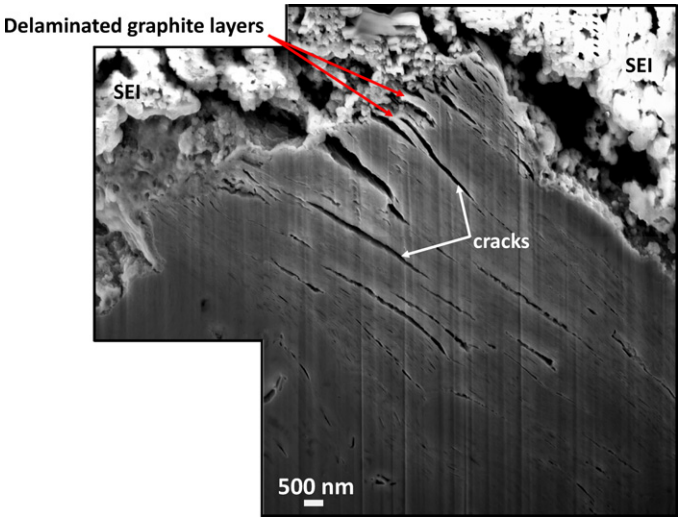

Fig. 6. Cross-sectional SEM image of the subsurface region (marked in Fig. 5(a)) of the graphite electrode cycled between 0.0 and 3.0 V at a linear scan rate of 5 mV s^{-1}, showing the presence of cracks resulting in partial delamination of graphite layers at the SEI/graphite interface.

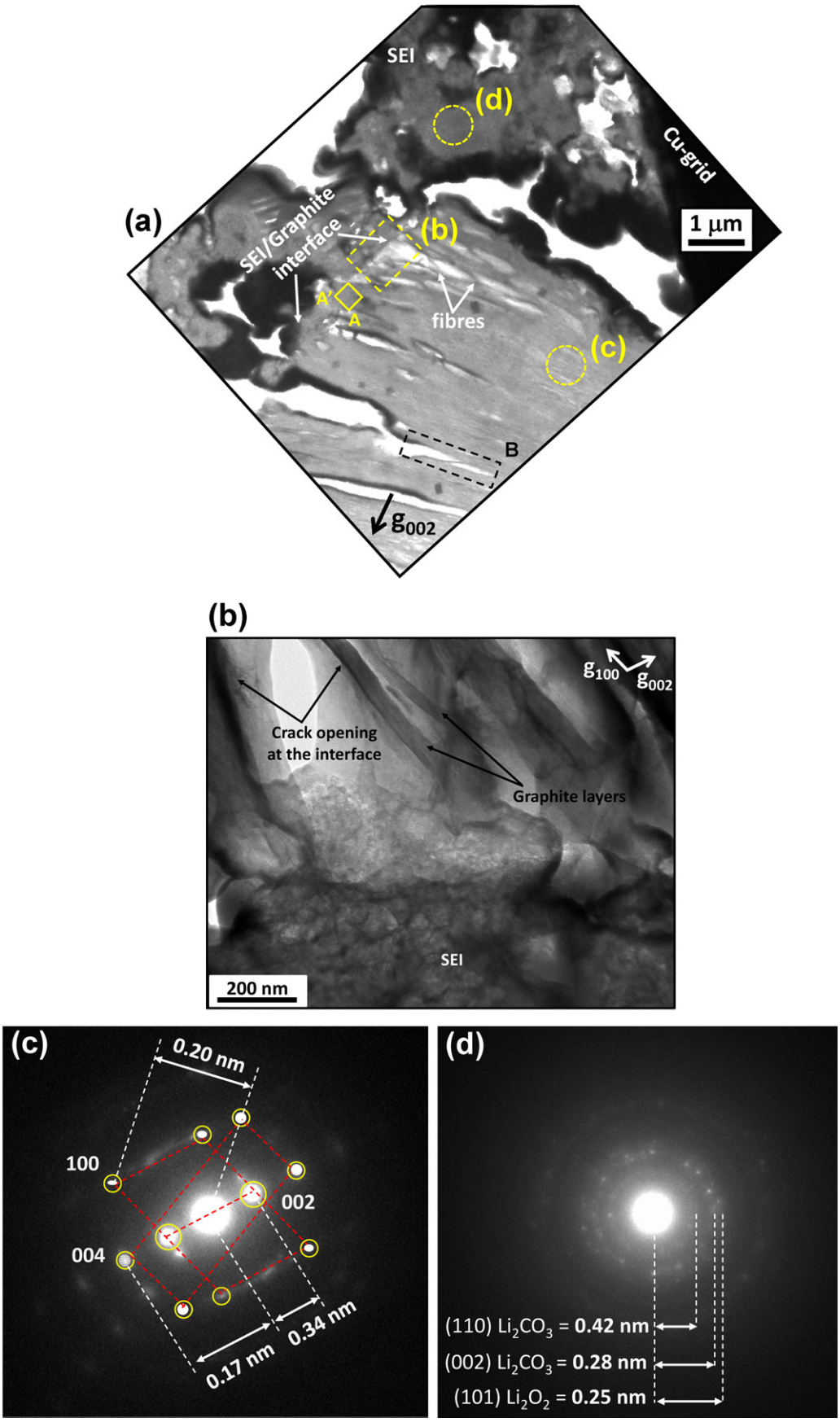

Fig. 7. (a) A low magnification, bright-field TEM image of the same region shown in Fig. 6, at the SEI/graphite interface. (b) High-magnification bright-field TEM image obtained from a region, marked as (b) in (a), revealing a granular appearance of the electrode/electrolyte interface. SAED patterns obtained from (c) a region [marked as (c) in (b)] in bulk graphite, and (d) from a region [marked as (d) in (a)] in the SEI layers.

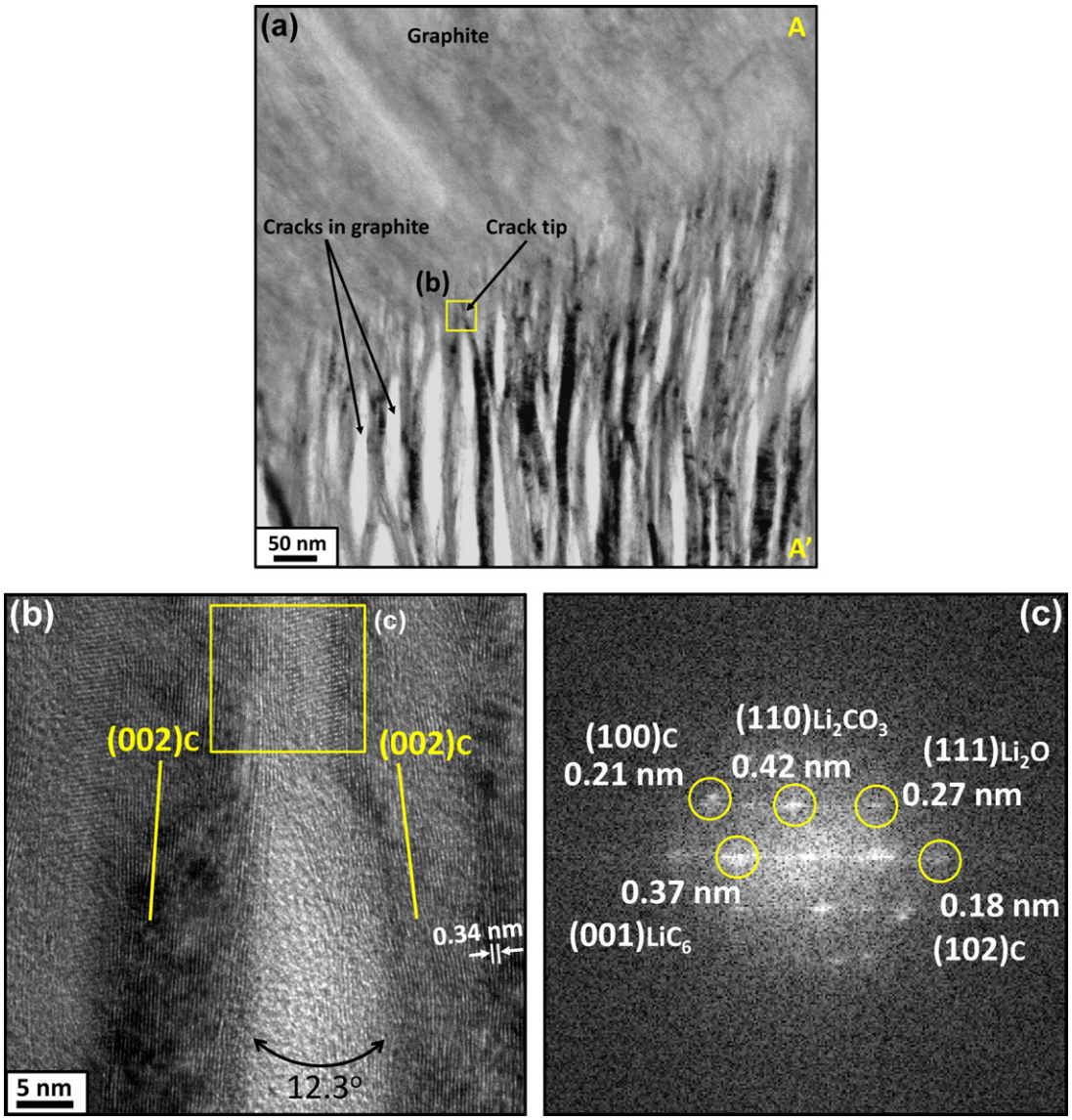

Fig. 8. (a) Bright field TEM image of electrochemically cycled graphite from a region close to the interface [marked as AA′ in Fig. 7 (a)] revealing graphite layer delamination initiated with the formation of crack tips. (b) HR-TEM image of the region, indicated as **(b)** in (a), revealed the point of separation of two graphite layers (consisting of graphene planes) and depicted the root of a crack. A tilt was observed between the crack faces, which consisted of the (0 0 2) planes of graphite. (c) Reduced FFT-derived diffraction pattern confirming the presence of Li–C compounds only at the root of layer separation as seen in (a).

surface by ion-milling trenches on either sides of it (Fig. 5(a)). A micro-manipulator with a tungsten-tip was placed at the top of the sample (Fig. 5(b)). The edges of the sample were then milled completely as shown in Fig. 5(c). The platelet, disconnected from rest of the graphite, was lifted out (Fig. 5(d)) and fixed to a Cu-grid (TEM sample holder). The sample was further milled to a final thickness of approximately 100 nm and then transferred to the TEM. A JEOL 2010F STEM was used to observe the cross-sectional microstructures at an operating voltage of 200 kV. A FEI Titan 80–300 TEM equipped with a hexapole-based aberration corrector for the image-forming lens, having a lateral resolution < 1 Å and operated at 300 kV, was used for high-resolution imaging of graphite layers.

3. Results and discussion

3.1. Observation of subsurface damage in cycled graphite electrodes

Fig. 6 shows a cross-sectional SEM image of the subsurface region of a graphite electrode cycled at a scan rate of 5 mV s^{-1}. This section was taken from the area marked in Fig. 5(a), where formation of interlayer cracks in graphite adjacent to the interface between graphite and SEI can be seen. The linear density of the cracks along the interface was measured as 2.83×10^{-3} nm^{-1}. These cracks extend parallel to each other and appeared to have caused partial delamination of graphite layers at the SEI/graphite interface at the locations indicated in Fig. 6. The morphology of the SEI layer formed at the interface can also be seen in the same figure. The SEI layer consisted of submicroscopic particles that were agglomerated and adhered to graphite surface. A bright-field TEM image of the same section shown in Fig. 6 is given in Fig. 7(a) where the boundary (interface) between graphite and the SEI is marked. Many graphite cracks propagated obliquely to the SEI/graphite interface for 2–3 μm. The cracks were partially separated and the crack faces were connected by a few strands or layers of graphite. These graphite layers, or fibres, indicated in Fig. 7(a) by arrows, appear to bridge the crack faces. Thus, the graphite crack growth process can be said to exhibit a quasi-ductile debonding behaviour rather than a cleavage-type brittle fracture [29] typically observed at the basal planes of graphite. Several typical damage

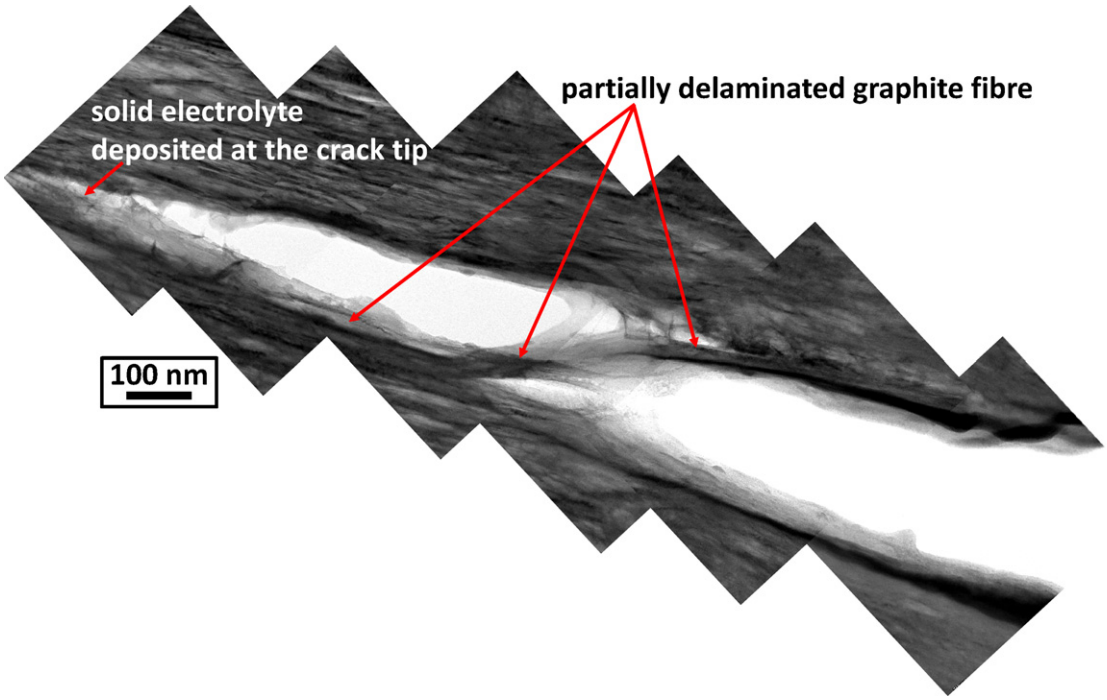

Fig. 9. A high magnification BF-TEM image revealing the deposition of SEI layers at the crack tip, and a typical example of a delaminated graphite layer marked as B in Fig. 7 (a) extending across the crack faces.

features of interest are marked in Fig. 7(a) and examined in more detail. Fig. 7(b) is a high-magnification bright-field TEM image, obtained from the area marked as (b) in Fig. 7(a), revealing the microstructure of electrode/electrolyte interface, where the cracks in graphite at this location were formed in the {1 0 0} direction (determined by the orientation of g_{100} vector) and approximately at 45–60° with respect to the interface. The interface between the graphite and the SEI layer consisted grains of nanocrystalline grains of 50–200 nm in diameter. SEI was found to deposit inside the crack. Fig. 7(c) is a selected area electron diffraction (SAED) pattern obtained from an undamaged region within graphite (marked as (c) in Fig. 7(a)) few microns away from the interface. Diffraction spots were obtained from different crystallographic planes of graphite with the highest intensity received from {0 0 2} family of planes having a *d*-spacing of 0.34 nm [30]. In addition, diffraction spots were obtained from {0 0 4} (*d*-spacing = 0.17 nm) and {1 0 0} (*d*-spacing = 0.20 nm) family of planes, again typical of pristine graphite planes. The diffraction conditions of the SEI and damaged graphite were also analyzed. A SAED pattern obtained from a region in the SEI layers (marked as (d) in Fig. 7(a)) is presented in Fig. 7(d). Analyses of the rings of diffraction spots revealed presence of crystallographic planes with *d*-spacings of 0.42 nm and 0.28 nm, which correspond to the {1 1 0} and {0 0 2} planes of Li_2CO_3 [31]. Diffraction ring patterns corresponding to a *d*-spacing of 0.25 nm were also identified in SEI, which could either be interpreted as corresponding to the {1 0 1} planes of Li_2O_2 [32] or to the {0 2 0} planes of Li_2CO_3. It is believed that the nanocrystalline grains observed at the interface contained these lithium compounds. The identification of {0 0 2} planes in Li_2CO_3 compound formed at the SEI/graphite interface is noteworthy as it was pointed out that lithium-ion diffusion would take place primarily through the (0 0 2) plane in Li_2CO_3 [33].

3.2. Characterization of subsurface cracks in graphite

A TEM image showing the tips of a group of fine cracks formed within the graphite in a region approximately 250–300 nm away

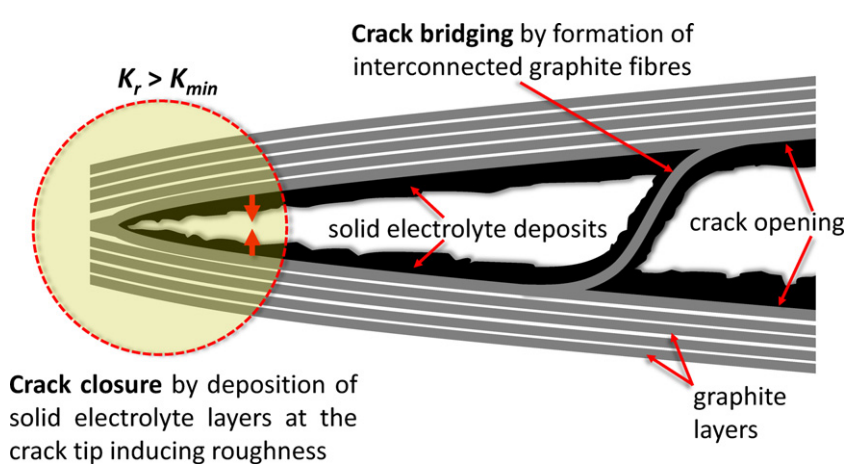

Fig. 10. A schematic showing the occurrence of mechanisms responsible for possible reduction in graphite crack growth; deposition of the co-intercalation compounds near the crack tip causing partial closure of crack, and crack face bridging by graphite fibres.

from the SEI/graphite interface (marked as AA′ in Fig. 7(a)) is given in Fig. 8(a). The crack faces maintained an almost parallel orientation with a crack opening displacement of 18 ± 5.7 nm. According to the HR-TEM image in Fig. 8(b) showing the structure of graphene planes near the crack tip (0 0 2) planes of graphite at each face of the crack formed a tilt angle of $12.3 \pm 0.25^{\circ}$, at a distance less than 100 nm from the crack tip. A reduced fast Fourier transform (FFT) derived diffraction pattern (Fig. 8(c)), obtained from the graphite layers at the tip of the crack, specifically from the region **(c)** in Fig. 8(b) identified the presence of lithium compounds. The lithium compounds identified near the crack tip included LiC_6, which was discerned by means of reflections from the {0 0 1} planes with a corresponding *d*-spacing of 0.37 nm [34]. Other compounds detected within the graphite lattice included Li_2CO_3 according to the reflections from the {1 1 0} planes with a *d*-spacing of 0.42 nm, and Li_2O according to the reflection from the {1 1 1} planes with a *d*-spacing of 0.27 nm. These observations serve to provide crystallographic evidence that lithium intercalation could be accompanied by solvent co-intercalation.

3.3. Mechanisms of crack formation and propagation during lithiation/de-lithiation

A well developed crack is shown in the high magnification bright field TEM image in Fig. 9. The crack shown in Fig. 9 is typical of many cracks of similar size observed in graphite and serves to illustrate some important aspects of crack growth mechanisms in electrochemically cycled graphite electrodes using voltage scan rates from 500 $\mu V\,s^{-1}$ to 5 $mV\,s^{-1}$ between 0.0 and 3.0 V. It is noted that very thin translucent but continuous layers of approximately 25–50 nm in thickness were formed at the crack tip and along the crack faces. These layers are believed to consist of lithium compounds (e.g., LiC_6, Li_2CO_3, and Li_2O) similar to those indentified for the crack in Fig. 8. The formation of these compounds indicate that solvent co-intercalation at the crack tip may play an important role in delaying graphite crack growth. Considering that graphite undergoes cyclic crack opening and closure processes under the stresses induced during lithiation and de-lithiation cycles [35–37], a fracture mechanics argument can be made to describe the graphite crack extension rate of a crack with length *a* per electrochemical cycle (da/dN), where dN consists of a complete voltage cycle ($0.0 \leftrightarrow 3.0$ V):

$$\frac{da}{dN} = C \cdot \Delta K^m \tag{1}$$

where ΔK ($=K_{max} - K_{min}$) is the cyclic stress intensity factor. In the presence of SEI deposits at the crack tip, crack flanks make physical contact at a high positive stress intensity value, $K_r > K_{min}$, in a way akin to the phenomenon known as roughness or asperity induced (K_r) crack closure [38]. Hence, the formation of the SEI deposits at the crack tip will cause crack flanks to reduce the effective ΔK value and, therefore, the graphite crack growth rate will be reduced proportional to the thickness of SEI. Further cyclic voltammetry tests with controlled ΔK values applied during lithiation and de-lithiation cycles will help to determine the graphite crack propagation rates. Once the growth behaviour of cracks that appear to be nucleated mostly during the first cycle is determined, the associated capacity loss due to graphite electrode degradation could be better understood.

Another mechanism that contributes to the reduction of graphite crack growth rate is attributed to bridging of faces of the crack by graphite layers or fibres. A representative example of graphite fibres connecting the two flanks of a crack is shown in Fig. 9. These fibres help to keep the graphite crack faces bridged together, thus increasing the stress intensity level needed to cause further growth.

In summary, the TEM observations on the propagating graphite cracks during electrochemical cycling at constant voltage scan rates identified two mechanisms, namely, crack closure and crack face bridging. These two mechanisms are shown schematically in Fig. 10, each contributing to the decrease of crack tip stress intensity and possibly playing a role in electrochemical cycling-induced degradation and loss of capacity of graphite electrodes.

4. Conclusions

Cyclic voltammetry tests were performed on graphite working electrodes to study the effect of the applied voltage on graphite damage. Graphite was cycled between 0.0 and 3.0 V vs. Li/Li^+ in an electrolyte composed of 1 M $LiClO_4$ in a 1:1 volumetric mixture of ethylene carbonate (EC) and 1,2-dimethoxy ethane (DME). FIB-milled Cross-sectional microstructures taken from the cycled graphite samples were used to observe the morphologies of graphite cracks formed during the cycling. The microstructural observations revealed some key mechanisms that control the formation and the propagation of cracks in graphite electrodes. The main conclusions are as follows:

1. Cross-sectional subsurface structure of cycled graphite revealed partial delamination of graphite layers at the SEI/graphite interface. Nanocrystalline grains observed within the SEI layer at the interface revealed the presence of Li_2CO_3.
2. Small cracks with tip angle of 12.3° were observed between the {0 0 2} planes of graphite about 250-300 nm away from the SEI/graphite interface. FFT-derived diffraction patterns revealed the presence of lithium compounds, LiC_6, Li_2CO_3 and Li_2O, incorporated in the graphite lattice preferentially at the root of graphite cracks.
3. Deposition of SEI layers at the crack tip possibly reduced the effective cyclic stress intensity factor, thereby decreasing crack growth rate. A crack bridging mechanism through the graphite fibres that interconnected the crack faces also provided resistance to crack propagation.

Acknowledgements

The authors would like to thank the Natural Sciences and Engineering Research Council of Canada (NSERC) for providing the financial support. Mr. F. Pearson, Ms. J. Huang and Dr. C. Andrei of Canadian Center of Electron Microscopy at McMaster University, Hamilton, Canada, are gratefully acknowledged for their assistance with the operation of electron microscopes. The authors thank Dr. X. Meng-Burany of the University of Windsor for useful discussions.

References

[1] L.B. Ebert, Annu. Rev. Mater. Sci. 6 (1976) 181–211.
[2] M.S. Dresselhaus, G. Dresselhaus, Adv. Phys. 30 (1981) 139–326.
[3] D. Fauteux, R. Koksbang, J. Appl. Electrochem. 23 (1993) 1–10.
[4] M. Winter, J.O. Besenhard, M.E. Spahr, P. Novak, Adv. Mater. 10 (1998) 725–763.
[5] S. Flandrois, B. Simon, Carbon 37 (1999) 165–180.
[6] X. Hongqi, F. Shibi, Y. Yingyan, Chin. Sci. Bull. 44 (1999) 385.
[7] D.D.L. Chung, J. Mater. Sci. 22 (1987) 4190.
[8] D. Aurbach, B. Markovsky, I. Weissman, E. Levi, Y. Ein-Eli, Electrochim. Acta 45 (1999) 67.
[9] M.E. Spahr, H. Buqa, A. Wursig, D. Goers, L. Hardwick, P. Novak, F. Krumeich, J. Dentzer, C. Vix-Guterl, J. Power Sources 153 (2006) 300–311.
[10] H. Buqa, A. Wursig, J. Vetter, M.E. Spahr, F. Krumeich, P. Novak, J. Power Sources 153 (2006) 385–390.
[11] G.C. Chung, H.J. Kim, S.I. Yu, S.H. Jun, J.W. Choi, M.H. Kim, J. Electrochem. Soc. 147 (2000) 4391.
[12] V.A. Sethuraman, L.J. Hardwick, V. Srinivasan, R. Kostecki, J. Power Sources 195 (2010) 3655.
[13] R. Kostecki, F. McLarnon, J. Power Sources 119–121 (2003) 550–554.
[14] E. Markervich, G. Salitra, M.D. Levi, D. Aurbach, J. Power Sources 146 (2005) 146–150.

[15] A. Naji, P. Willmann, D. Billaud, Carbon 36 (1998) 1347–1352.
[16] E. Peled, J. Electrochem. Soc. 126 (1979) 2047–2051.
[17] E. Peled, Lithium Stability and Film Formation in Organic and Inorganic Electrolytes for Lithium Battery Systems, Academic, London, 1983.
[18] H. Zhang, F. Li, C. Liu, J. Tan, H. Cheng, J. Phys. Chem. B 109 (2005) 22205–22211.
[19] D. Aurbach, E. Zinigrad, Y. Cohen, H. Teller, Solid State Ionics 148 (2002) 405–416.
[20] M. Winter, K.-C. Moeller, J.O. Besenhard, in: G.-A. Nazri, G. Pistoia (Eds.), Lithium Batteries Science and Technology, Kluwer Academic, Dordrecht, 2003.
[21] D. Aurbach, B. Markovsky, A. Shechter, Y. Ein-Eli, H. Cohen, J. Electrochem. Soc. 143 (1996) 3809–3820.
[22] Y. Tian, A. Timmons, J.R. Dahn, J. Electrochem. Soc. 156 (2009) A187–A191.
[23] S.J. Harris, A. Timmons, D.R. Baker, C. Monroe, Chem. Phys. Lett. 485 (2010) 265–274.
[24] S. Bhattacharya, A.R. Riahi, A.T. Alpas, Scripta Mater. 64 (2011) 165–168.
[25] N. Kambe, M.S. Dresselhaus, G. Dresselhaus, S. Basu, A.R. McGhie, J.E. Fischer, Mater. Sci. Eng. 40 (1979) 1–4.
[26] X. Song, K. Kinoshita, T. Tran, J. Electrochem. Soc. 143 (1996) L120–L123.
[27] K. Kinoshita, J. Bonevich, X. Song, T. Tran, Solid State Ionics 86–88 (1996) 1343–1350.
[28] K. Sato, M. Noguchi, A. Demachi, N. Oki, M. Endo, Science 264 (1994) 556–558.
[29] M.W. Barsoum, A. Murugaiah, S.R. Kalidindi, T. Zhen, Y. Gogotsi, Carbon 42 (2004) 1435–1445.
[30] M. Bagouin, D. Guérard, A. Hérold, Compt. Rend. Hebd. Séances Acad. Sci., Ser. C 262 (1966) 557–559.
[31] J. Zemann, Acta Crystall 10 (1957) 664–666.
[32] H. Föppl, Z. Anorg. Allg. Chem 291 (1957) 12–50.
[33] J. Mizusaki, H. Tagawa, K. Saito, K. Uchida, M. Tezuka, Solid State Ionics 53–56 (1992) 791–797.
[34] A.H. Whitehead, K. Edström, N. Rao, J.R. Owen, J. Power Sources 63 (1996) 41–45.
[35] Y.T. Cheng, M.W. Verbrugge, J. Electrochem. Soc. 157 (2010) A508–A516.
[36] Y.T. Cheng, M.W. Verbrugge, Electrochem. Solid State Lett. 13 (2010) A128–A131.
[37] R. Deshpande, Y.T. Cheng, M.W. Verbrugge, A. Timmons, J. Electrochem. Soc. 158 (2011) A718–A724.
[38] S. Suresh, G.F. Zamiski, R.O. Ritchie, Metall. Trans. A 12A (1981) 1435–1443.